

Automatic Robot Hand-Eye Calibration Enabled by Learning-Based 3D Vision

Leihui Li^a, Xingyu Yang^a, Riwei Wang^b, Xuping Zhang^a

^aDepartment of Mechanical and Production Engineering, Aarhus University, Aarhus, Denmark

^bSchool of Data Science and Artificial Intelligence, Wenzhou University of Technology, Wenzhou, China

Abstract

Hand-eye calibration, as a fundamental task in vision-based robotic systems, aims to estimate the transformation matrix between the coordinate frame of the camera and the robot flange. Most approaches to hand-eye calibration rely on external markers or human assistance. We proposed a novel methodology that addresses the hand-eye calibration problem without external calibration objects or human support, but with the robot base. Using point clouds of the robot base, a transformation matrix from the coordinate frame of the camera to the robot base is established as “ $\mathbf{I}=\mathbf{AXB}$.” To this end, we exploit learning-based 3D detection and registration algorithms to estimate the location and orientation of the robot base. The robustness and accuracy of the method are quantified by ground-truth-based evaluation, and the accuracy result is compared with other 3D vision-based calibration methods. To assess the feasibility of our methodology, we carried out experiments utilizing a low-cost structured light scanner across varying joint configurations and groups of experiments. The proposed hand-eye calibration method achieved a translation deviation of 0.930 mm and a rotation deviation of 0.265 degrees according to the experimental results. Additionally, the 3D reconstruction experiments demonstrated a rotation error of 0.994 degrees and a position error of 1.697 mm. Moreover, our method offers the potential to be completed in 1 second, which is the fastest compared to other 3D hand-eye calibration methods. Code is released at github.com/leihui6/LRB0.

Keywords: Hand-Eye Calibration, 3D Registration, 3D Detection, Point Cloud, 3D Reconstruction

1. Introduction

Hand-eye calibration [1, 2, 3], as one of the essential parts of robot manipulation [4, 5, 6, 7], refers to estimating a relative rigid relationship between the robot end-effector (hand) and its sensor (eye), typically a camera. This relationship consists of a rotation and translation matrix, and can be used to align the hand in the robotic system with its visual perception, enabling the robot to manipulate objects in its environment accurately. Three dimension (3D) and two dimension (2D)-based vision has become increasingly prevalent in robot manipulation [8, 9, 10, 11], and hand-eye calibration problem has been widely studied [12, 13, 14]. In this paper, we focus on 3D-based vision where point cloud data are only used for the hand-eye calibration problem.

In general, accurate calibration objects and generating multiple robot poses are always required during hand-eye calibration. For hand-eye calibration based on 2D (RGB) images, the correspondence between 3D spatial coordinates and 2D image coordinates is achieved by using some known feature points on the calibration object [15]. The required calibration objects can be chessboards [16] and specific labels [17, 18]. More specifically, the end-effector of the robot is needed to move to a series of known positions, and the data are collected in the form of images and end-effector poses. In the end, the collected data are used to estimate the transformation matrix. Furthermore, for approaches based on the point cloud or depth image, 3D objects are utilized, such as a 3D cube [19] and a standard sphere [15]. The existing hand-eye calibration approaches are faced with several key challenges: 1) they always require an additional calibration object; 2) they are time-consuming due to the multiple movements of the robot; 3) human support is required during calibration process. While hand-eye calibration is typically considered a one-time task, recalibrations are necessary and can be challenging for numerous robots integrated with a vision system. Moreover, the parameters of a robotic system changing over time can affect the calibrated relative position between the camera and the end-effector, such as wear and tear [20], component replacement, environmental changes [21], and a specific

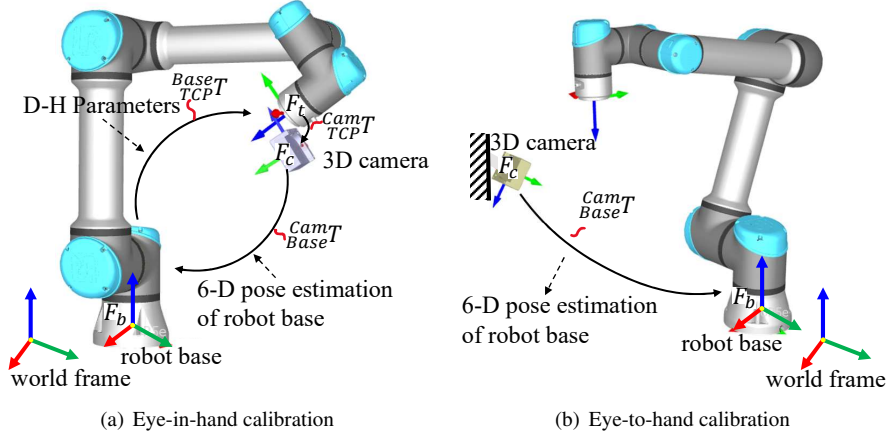


Figure 1: Our proposed hand-eye calibration method. We estimate the transformation matrix between the robot base and camera frame using point clouds and one robot arm movement where the robot base as an object is detected and aligned with a 3D model.

vibration [22] during movement for mobile robots. Therefore, fast and reliable hand-eye calibration/recalibration is necessary for vision-guide robot systems.

To overcome these drawbacks, this paper proposes a method for solving hand-eye calibration with point clouds and one robot arm movement. We use the robot base as the calibration object to eliminate the need for additional equipment, making it more efficient and out-of-the-box. Given point clouds of the robot base, the position and orientation of the robot base are estimated relative to the frame of the 3D camera. For this purpose, our method involves detecting the robot base and aligning it with a corresponding 3D model in the form of point cloud. This process can finally determine the transformation between the camera frame and the robot base, $^{Cam}Base^T$. In the case of eye-in-hand calibration, the transformation between the camera and the robot flange or more specifically, the tool center point (TCP), $^{Cam}TCP^T$, can be calculated by an inverse matrix operation, as shown in Fig. 1(a). In the case of eye-to-hand calibration, the transformation between the robot base and the camera frame, $^{Cam}Base^T$, can be estimated directly, as shown in Fig. 1(b).

Our hand-eye calibration framework only needs one robot arm movement and one frame point cloud for the robot base. In other words, it does not require external calibration objects or human support, but the robot base during calibration. Given a depth camera, users or customers can start their calibration-required applications when their robot is placed in service, named as an out-of-the-box feature. In this paper, the robustness and accuracy of our proposed method are thoroughly considered and evaluated through experiments with a UR5e and a structured light camera, which are widely used in industry [23, 24, 25]. The contributions of this work are as follows:

- We present a novel hand-eye calibration approach which uses the native object, the robot base, as the calibration object and requires only point clouds of the robot base and a robot arm movement.
- We adopt and integrate a learning-based 3D detection and registration framework, in which methods for data preparation and evaluation are provided and a method for generating low-overlap point cloud dataset in a virtual environment is given as well.
- We conduct the 3D reconstruction experiments to evaluate the robustness and accuracy of our proposed methods, including calibration at multiple joint configurations and the 3D reconstruction of a plane and a hemispherical object.

The remaining part of the paper is organized as follows: In Section 2, we review the related work on hand-eye calibration. The proposed method is described in detail in Section 3. Section 4 presents the implementation details and evaluation for the learning-based detection and registration algorithm. In Section 5, we evaluate the robustness and accuracy of our method through ground-truth-based experiments. Finally, Section 6 summarises the main conclusions and discusses future work.

2. Related work

Various methods have been proposed to address the hand-eye calibration problem, ranging from traditional approaches using RGB images to more recent methods incorporating 3D data. For methods that rely on 2D images as input, the procedure typically involves capturing a series of images from different viewpoints, each containing calibration patterns. Current hand-eye calibration methods can be broadly classified into four mathematical models [13]: “ $\mathbf{AX}=\mathbf{XB}$ ” [1, 26], “ $\mathbf{AX}=\mathbf{YB}$ ” [27, 28], “ $\mathbf{AXB}=\mathbf{YCZ}$ ” [29, 30] and reprojection error-based calibration (REC) [31, 32, 33].

In the forms of “ $\mathbf{AX}=\mathbf{XB}$ ” and “ $\mathbf{AX}=\mathbf{YB}$,” calibration objects are utilized to establish the camera-world frame. The form of “ $\mathbf{AXB}=\mathbf{YCZ}$ ” is used for multiple robots, while markers on the robot flange are required. Calibration patterns such as checkerboard [34], ArUco [35], ARToolKit [36], and ARTag [37] are commonly used. Previous works related to “self-calibration” mainly rely on REC, motion estimation [38, 39, 40, 41, 33], and tool-tracking [42]. Although these methods do not rely on special calibration objects, they cannot easily be used in a non-rigid environment where the geometry of the targets is unknown [42]. Moreover, existing methods typically require a minimum of two movements to achieve calibration, and additional movements may be necessary to improve accuracy [2, 3].

With the availability of affordable 3D cameras, an increasing number of applications are incorporating 3D sensors that can generate both depth images and point clouds. Their hand-eye calibration problem was still solved with calibration patterns. For example, a criterion sphere [19], 3D cube [15], the planner-like object [43] and pin-like object [44] are utilized in 3D vision-based hand-eye calibration. However, these methods require high-quality manufacturing of the calibration objects and are practically inappropriate for many application due to the complex operations for calibration.

In addition to methods that use designed calibration objects, a calibration method utilizing arbitrary objects was introduced by [8] and [45], which employs a modified iterative closest point algorithm to align the point clouds captured at different robot poses. Our proposed method is similar to theirs. However, the calibration object in our method is the robot base rather than a third-party object. In addition, instead of having many robot poses in the hand-eye calibration process, only one is needed. Specifically, we build a transformation matrix as “ $\mathbf{I}=\mathbf{AXB}$,” where \mathbf{A} denotes the forward kinematics whose parameters are supposed to be known, and \mathbf{B} is estimated by point cloud registration. \mathbf{X} is unknown and represents the transformation matrix between the robot flange and the camera. We can calculate \mathbf{X} straightforwardly by the inverse operation.

There have been some similar works aimed at estimating the pose of robotic arms. One such work was presented by [46], where camera-to-robot pose estimation from a single RGB image is achieved. Another related approach is proposed by [47], which estimates the pose of a marker-less robot arm using only one frame of depth image, making one-shot hand-eye calibration possible without external calibration objects. It is worth noting that one approach, seline [48]¹, estimates the transformation between the robot base and the camera frame by estimating the pose of the robot’s end effector in the camera optical frame. However, these methods may not be easily adaptable to eye-in-hand calibration, as it can be difficult to capture the end-effector in the camera frame. In contrast, our proposed method utilizes point clouds of the robot base and can be used for eye-in-hand calibration.

In summary, our proposed approach has the following features: 1) use of a native calibration object: robot base; 2) it only requires one robotic movement; 3) it only needs point clouds of the robot base.

3. Problem Definition and Methodology

In this section, we first define the hand-eye calibration problem, including both eye-in-hand and eye-to-hand calibration, and present the classical solutions “ $\mathbf{AX}=\mathbf{XB}$ ” for each. Then a detailed explanation of our proposed method is provided.

¹<https://github.com/jaymwong/seline>

3.1. Hand-eye Calibration

There are various coordinate systems in the field of robotics, such as the robot base, sensors and tool center point (TCP) or robot flange. In order to perform robot tasks accurately, it is crucial to understand the rigid relationship between these coordinate systems. Hand-eye calibration is a technique used to determine the transformation matrix between the robot base and the camera frame, allowing this information to be integrated into other parts of the robotic system. As shown in Fig. 1, the robot base coordinate system is defined as F_b , and the camera frame is defined as F_c . The image data, such as 2D images and point clouds, are collected in the camera coordinate system. The transformation between F_c and F_b needs to be estimated to perform vision-guided action. In general, depending on whether the camera is mounted on a robot arm, there are two kinds of hand-eye calibration, known as eye-in-hand and eye-to-hand calibration.

3.2. Eye-in-Hand Calibration

Eye-in-hand calibration involves mounting cameras, either 2D or 3D, on a robotic arm. The objective of this calibration is to determine the rigid transformation matrix from the TCP to the camera's coordinate frame. The ${}^{TCP}_{Cam}\mathbf{T}$ consists of a matrix of rotation ($\mathbf{R}_{3\times3}$) and translation ($\mathbf{t}_{3\times1}$) as

$${}^{TCP}_{Cam}\mathbf{T} = \begin{pmatrix} \mathbf{R}_{3\times3} & \mathbf{t}_{3\times1} \\ \mathbf{0}_{1\times3} & 1 \end{pmatrix} \quad (1)$$

To solve ${}^{TCP}_{Cam}\mathbf{T}$, a common method “ $\mathbf{AX} = \mathbf{XB}$ ” was presented, which use the unvaried transformation between the calibration object and robot base, i.e., the ${}^{Base}_{Obj}\mathbf{T}$ is consistent. At i^{th} and $i+1^{th}$ pose, calibration object in camera frame is recorded as ${}^{Cam}_{Obj}\mathbf{T}_i$ and ${}^{Cam}_{Obj}\mathbf{T}_{i+1}$, such that we have

$$\begin{cases} {}^{Base}_{TCP}\mathbf{T}_i {}^{TCP}_{Cam}\mathbf{T} {}^{Cam}_{Obj}\mathbf{T}_i = {}^{Base}_{TCP}\mathbf{T}_{i+1} {}^{TCP}_{Cam}\mathbf{T} {}^{Cam}_{Obj}\mathbf{T}_{i+1} \\ \vdots \\ {}^{Base}_{TCP}\mathbf{T}_{n-1} {}^{TCP}_{Cam}\mathbf{T} {}^{Cam}_{Obj}\mathbf{T}_{n-1} = {}^{Base}_{TCP}\mathbf{T}_n {}^{TCP}_{Cam}\mathbf{T} {}^{Cam}_{Obj}\mathbf{T}_n \end{cases} \quad (2)$$

where ${}^{TCP}_{Cam}\mathbf{T}$ can be assumed as a constant value, and n denoted the number of robot motion. At the i^{th} and $i+1^{th}$ pose, a formula of “ $\mathbf{AX}=\mathbf{XB}$ ” can be derived by

$$\underbrace{{}^{Base}\mathbf{T}_{i+1}^{-1} {}^{Base}\mathbf{T}_i}_{\mathbf{A}} \underbrace{{}^{TCP}_{Cam}\mathbf{T}}_{\mathbf{X}} = \underbrace{{}^{TCP}_{Cam}\mathbf{T}}_{\mathbf{X}} \underbrace{{}^{Cam}\mathbf{T}_{i+1} {}^{Cam}\mathbf{T}_i^{-1}}_{\mathbf{B}} \quad (3)$$

where ${}^{TCP}_{Cam}\mathbf{T}$ can be estimated by nonlinear solver [2], Euclidean group [49], dual quaternions [50, 51], Kronecker product [41, 52], linear equations [53] and optimized neural network [54] etc.

However, our method proposes a simpler rigid relationship by estimating the 6D pose of the robot base with respect to the camera frame. It eliminates the need for multiple movements during the hand-eye calibration process. To be more specific, the relationship is “ $\mathbf{I}=\mathbf{AXB}$ ” which can be explained as

$$\mathbf{I} = \underbrace{{}^{Base}\mathbf{T}}_{TCP} \underbrace{{}^{TCP}_{Cam}\mathbf{T}}_{Cam} \underbrace{{}^{Cam}_{Base}\mathbf{T}}_{Base} \quad (4)$$

where ${}^{Base}_{TCP}\mathbf{T}$ can be determined through the D-H model that is supposed to be known, while the ${}^{Cam}_{Base}\mathbf{T}$ is obtained through 6D pose estimation for the robot base in our work, as illustrated in Fig. 1(a). As a result, ${}^{TCP}_{Cam}\mathbf{T}$ can be derived directly as

$${}^{TCP}_{Cam}\mathbf{T} = \underbrace{{}^{Base}_{TCP}\mathbf{T}}_{TCP}^{-1} \underbrace{{}^{Cam}_{Base}\mathbf{T}}_{Base} \quad (5)$$

3.3. Eye-to-Hand Calibration

Eye-to-hand calibration refers to a camera mounted stationary outside the robot, where the camera can have a global view of the workspace. The purpose of eye-to-hand calibration is to determine a rigid transformation matrix

between the camera frame and the robot base frame (${}_{Base}^{Cam}\mathbf{T}$). We use the consistent displacement from a calibration object to the robot flange. By attaching a calibration object to the robot flange, we have

$$\begin{cases} {}_{Base}^{TCP}\mathbf{T}_i {}_{Cam}^{Base}\mathbf{T} {}_{Obj}^{Cam}\mathbf{T}_i = {}_{Base}^{TCP}\mathbf{T}_{i+1} {}_{Cam}^{Base}\mathbf{T} {}_{Obj}^{Cam}\mathbf{T}_{i+1} \\ \vdots \\ {}_{Base}^{TCP}\mathbf{T}_{n-1} {}_{Cam}^{Base}\mathbf{T} {}_{Obj}^{Cam}\mathbf{T}_{n-1} = {}_{Base}^{TCP}\mathbf{T}_n {}_{Cam}^{Base}\mathbf{T} {}_{Obj}^{Cam}\mathbf{T}_n \end{cases} \quad (6)$$

where n denotes the number of robot motion and \mathbf{T}_i denotes the rigid transformation corresponding to the i^{th} robot motion. Similar with eye-in-hand calibration, Eq.6 also can be represented as Eq.7 at i^{th} and $i + 1^{th}$ pose.

$$\underbrace{{}_{Base}^{TCP}\mathbf{T}_{i+1}^{-1} {}_{Base}^{TCP}\mathbf{T}_i}_{A} \underbrace{{}_{Cam}^{Base}\mathbf{T}}_X = \underbrace{{}_{Cam}^{Base}\mathbf{T}}_X \underbrace{{}_{Obj}^{Cam}\mathbf{T}_{i+1} {}_{Obj}^{Cam}\mathbf{T}_i^{-1}}_B \quad (7)$$

where ${}_{Base}^{TCP}\mathbf{T}$ can be provided by a robotic kinetic model, and ${}_{Obj}^{Cam}\mathbf{T}$ is obtained from the feature detection result of images. It is necessary to have at least two robot motions to uniquely solve for \mathbf{X} . Meanwhile, a greater number of motions n may be required to achieve a higher level of accuracy [2, 3].

Our proposed eye-to-hand calibration differs from conventional methods in that it directly estimates the 6D pose of the robot base. Specifically, the rotation and translation of the robot base is determined with respect to the camera frame, which is what eye-to-hand calibration estimates, i.e., ${}_{Base}^{Cam}\mathbf{T}$ in Eq.4. In addition, in practice the camera is positioned adjacent to the robot and has an overall view of the workspace, such that the transformation between the camera and robot base, ${}_{Base}^{Cam}\mathbf{T}$, can be determined from point clouds with one robot arm movement, as depicted in Fig. 1(b).

3.4. 6D-Pose Estimation of Robot Base

The objective of eye-in-hand calibration is to estimate the transformation matrix between the coordinate frame of the camera and the TCP using Eq.5. On the other hand, the goal of eye-to-hand calibration is to find the transformation matrix between the coordinate frame of the camera and the robot base (${}_{Base}^{Cam}\mathbf{T}$). They all require the estimation of the transformation matrix between the robot base and the camera frame, which is a common step in both calibrations. In our work, it is solved as a 6D pose estimation problem for the robot base.

Our developed pipeline for robot base 6D-pose estimation is depicted in Fig. 2. The pipeline consists of three steps. Firstly, the robot base is detected and extracted using a single point cloud as the region of interest (RoI), which is obtained by performing one robot arm movement. Secondly, the extracted point cloud is registered with a robot base model, serving as a reference data. Lastly, the position and rotation matrix of the robot base are determined with respect to the camera frame.

More specifically, a point cloud captured in the camera frame is transformed into the robot base model frame by ${}_{Model}^{Cam}\mathbf{T}$. Meanwhile, a robot base RoI is extracted from this frame. Thus, the RoI and the robot base model are in the same coordinate system. In addition, the robot base model is a reference data in the registration task. Therefore, we have a transformation matrix between the camera frame and the reference data as

$${}_{Ref}^{Cam}\mathbf{T} = {}_{Model}^{Cam}\mathbf{T} {}_{Ref}^{RoI}\mathbf{T} \quad (8)$$

where ${}_{Model}^{Cam}\mathbf{T}$ is known and consists of a series of scaling, rotation, and translation manipulations to make our data feasible in the 3D detection framework. ${}_{Ref}^{RoI}\mathbf{T}$ can be obtained from the point cloud registration framework. A translation vector from the camera frame to the robot base frame is given by Eq.9

$${}_{Base}^{Cam}\mathbf{t} = {}_{Ref}^{Cam}\mathbf{T} \cdot \mathbf{P}_0 \quad (9)$$

where $\mathbf{P}_0 = \{0, 0, 0, 1\}$ is an origin point in the reference point cloud (robot base model). A vector containing the first three elements in ${}_{Base}^{Cam}\mathbf{t}$ is considered a translational matrix. A rotation matrix of the RoI with respect to the camera frame is then obtained by

$${}_{Base}^{Cam}\mathbf{R} = norm({}_{Ref}^{Cam}\mathbf{R}) \cdot \mathbf{R}_z(-\theta_1) \quad (10)$$

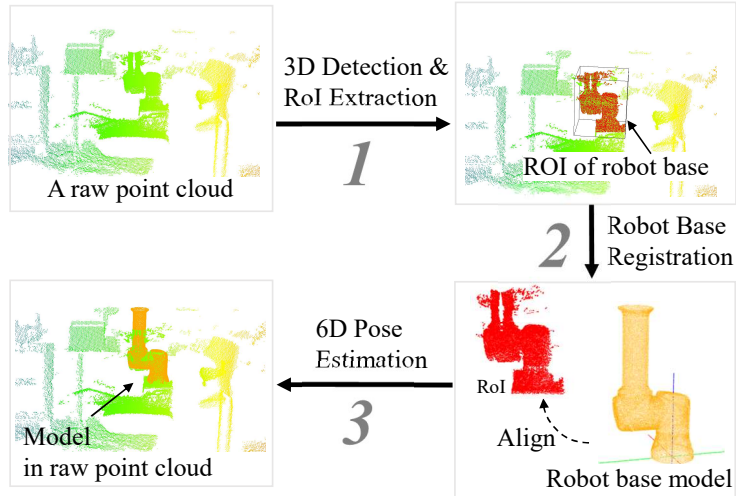


Figure 2: Our developed pipeline for the robot base 6D-Pose estimation which involves detecting the robot base as a ROI within point clouds, followed by a registration method that aligns a reference 3D model with the ROI. Finally, the transformation matrix can be calculated by the registration result.

Table 1: D-H parameter table for the UR5e robot

Kinematics	a_{i-1} (m)	α_{i-1} (rad)	d_i (m)	θ_i
Joint1	0	0	0.1625	θ_1
Joint2	0	pi/2	0	θ_2
Joint3	-0.425	0	0	θ_3
Joint4	-0.392	0	0.1333	θ_4
Joint5	0	pi/2	0.0997	θ_5
Joint6	0	- pi/2	0.0996	θ_6

where *norm* is the normalisation for each row in ${}^{Cam}_{Ref}\mathbf{R}$, which is a rotation matrix of ${}^{Cam}\mathbf{T}_{Ref}$. $\mathbf{R}_z(\cdot)$ denotes a rotation matrix along the Z-axis, θ_1 is the rotation angle of the first joint. So far, we can express the transformation matrix between the camera and robot base frame as Eq.11, the 6D pose of robot base relative to the camera frame.

$${}^{Cam}_{Base}\mathbf{T} = \begin{pmatrix} norm({}^{Cam}_{Ref}\mathbf{R}) \cdot \mathbf{R}_z(-\theta_1) & {}^{Cam}\mathbf{T}_{Ref} \cdot \mathbf{P}_0 \\ \mathbf{0}_{1 \times 3} & 1 \end{pmatrix} \quad (11)$$

In addition, a transformation between the robot flange and the robot base must be determined. In our study, this can be achieved using a Denavit-Hartenberg (D-H) parameter model. Specifically, our study applies it to a UR5e robot, as shown in Table 1.

There are many joint configurations for capturing the robot base. To make the robot base easy to detect and consistent with the 3D model where the second joint is fixed -90.0, we fix the second joint of the robot base at -90.0 degrees during hand-eye calibration with the UR5e. Other angles are possible if they can avoid symmetry problems and capture the geometric features of the robot base. For example, 0.0 degrees for the second joint can provide alignable data. For other robots, the configuration of specific joints can be determined based on their respective models. Therefore, the inclusion of a second joint in the robot base is essential to overcome potential symmetry-related challenges during the registration process. Relying solely on first joint data makes it difficult to identify the rotation and translation accurately, especially when dealing with cylindrical objects, where the rotation and translation matrix may be uncertain.

The UR5e robot model utilized in our study is obtained from the official Universal Robots website. A sampling tool provided by Cloudcompare [55] is used to convert the 3D mesh into point cloud. It is worth noting that the coordinate

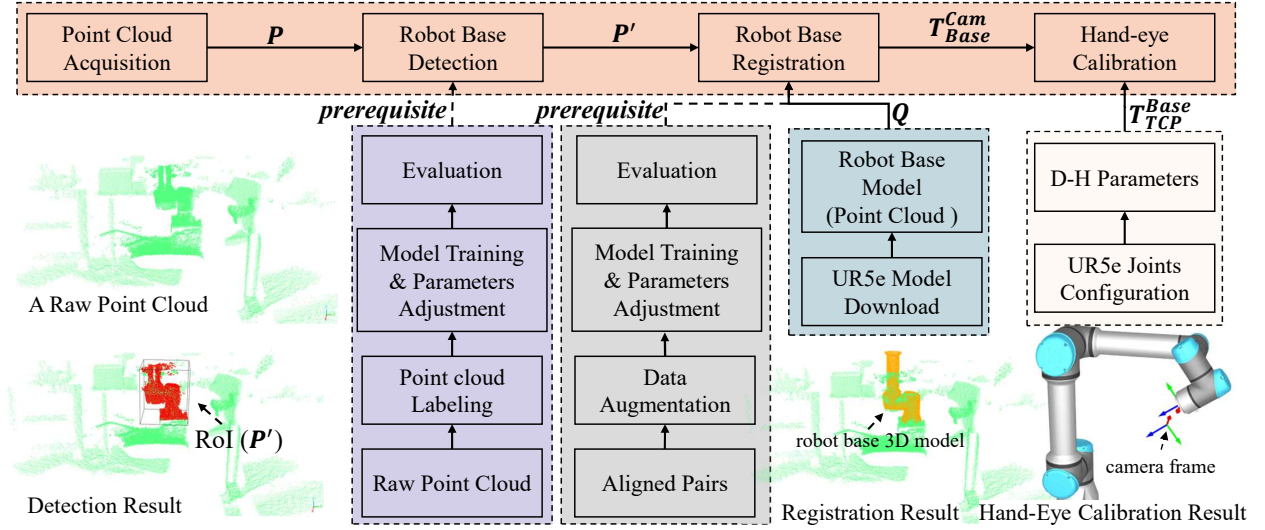


Figure 3: Overview of our proposed method. Given a point cloud (\mathbf{P}) from a 3D camera, the robot base is detected and located as an RoI (\mathbf{P}') via a learning-based 3D detection framework PV-RCNN++, which is trained and evaluated with our real-world dataset for the robot base task. In addition, the number of training datasets for robot base registration is increased by point cloud augmentation using a small number of aligned point clouds. We adopted a low-overlap designated learning-based framework, PREDATOR, to align the RoI with a 3D model (\mathbf{Q}) of the robot base. The performance of the registration is also evaluated with our real data. Finally, the hand-eye calibration is solved with the registration result (T_{Base}^{Cam}) and the D-H parameter model (T_{TCP}^{Base}).

system of the UR5e model is consistent with the real UR5e robot. In other words, the origin and coordinate system of the first joint are at the bottom of the robot base.

4. Implementation

In this section, our proposed method is implemented. The developed framework is illustrated in Fig. 3. We employ a learning-based 3D detection and registration method, which is specifically introduced and evaluated for hand-eye calibration tasks. We use real point clouds acquired by a structured light camera (LIPSedge™ L215u)² to build our training and evaluation datasets. As described in the manufacturer’s product manual, the camera has several key features: 1) up to 0.3% at 100cm accuracy with depth resolution 1280*800; 2) FoV 50° x 74° x 84° with range 0.3 to 1 m; 3) 640x480 depth output at 60fps. In addition, our experiment shows that it produces point clouds with a density of 0.9 mm within a working distance of 50 cm. The output format of the camera is simply a file containing at least the X, Y and Z values.

Moreover, in our study, the 3D camera is mounted on a gripper which is attached to the robot flange. The UR5e used in the experiments has been factory calibrated, and the intrinsic parameters of the camera were determined offline.

4.1. Robot Base Detection

The robot base detection is introduced in terms of data preparation, training performance, and detection evaluation. Data preparation encompasses acquiring point cloud data and describing the system setup and equipment used. We provide details about the training process and evaluate the performance of the detection module.

Robot base detection aims to find a bounding box for the robot base given a single point cloud. A 3D detection module is needed before robot base registration because: 1) points representing the robot base are extracted to improve the overlap ratio with the model; 2) we assume that the relative relationship between the robot base and the camera is uncertain in an unknown environment. Therefore, a reliable, robust, and accurate 3D detection solution is necessary.

²<https://www.lips-hci.com/>

An improved and state-of-art work PV-RCNN++ [56]³, which is a more practical framework for real-world applications, is exploited in our method for robot base detection. It improves the PV-RCNN [57] framework by introducing a sectorized proposal-centric keypoint sampling strategy and VectorPool aggregation module. Specifically, the Sectorized Prosoal Centric(SPC) uniformly sampled keypoints from neighboring regions. The keypoint candidates P' are restricted as Eq.12 given the neighboring point sets:

$$P' = \{p_i \mid \|p_i - c_j\| < 0.5 \cdot \max(d_j) + r^{(s)}\} \quad (12)$$

where c_j and d_j are the center and size of each proposal box. $r^{(s)}$ denotes a hyperparameters for the maximum extended radius of proposals. A VectorPool module is designated to preserve the spatial point distribution of local neighborhoods by encoding different spatial regions. The computation complexity and demanded memory resources are reduced after these adjustments. The experiments show that PV-RCNN++ achieved remarkable performance on large-scale open datasets such as KITTI [58] and Waymo [59] open dataset, which are widely used and currently the largest dataset with LiDAR point clouds for 3D object detection of autonomous driving. We adopted our raw data to the format used in the KITTI dataset.

4.1.1. Data Preparation

A total of 1170 point clouds of the UR5e robot base are captured and preprocessed by applying scaling and transformation operations, which enables our data trainable. Furthermore, the labels of the robot base are annotated on an online platform⁴, where we manually select a 3D box to encompass the robot base. This labeling approach can be applied to other robot bases as well. We use 40% of the total point cloud for evaluation, while the remaining 60% is used for model training. Data preparation for robot base detection is performed offline and does not take time away from hand-eye calibration in practice.

4.1.2. Training Performance

In order to prepare the data for training, the following parameters are set: 1) range of point cloud: [-12m, 12m], [-12m, -12m], and [-2m, 4m] along X, Y, and Z axes; 2) voxel for our point clouds: [0.5,0.5,0.15]; 3) batch size and epoch: 4 and 1000. A GTX3090 GPU card is utilized for training.

Regarding the training process, the learning rate is reduced from 0.001 to 1e-7 with cosine annealing during more than 0.17 million iterations, as illustrated in Fig. 4(a). The training process takes approximately 37 hours. The loss for PV-RCNN++ consists of the region proposal, key segmentation and the proposal refinement loss, which learns to predict the size and position offsets relative to the proposal box. The change in the proposal refinement loss value during the training process is shown in Fig. 4(b), with a blue curve for the change in loss. The final loss value is approximately 0.164.

4.1.3. Evaluation

We evaluated our trained model using more than 400 point clouds, to test the predicted results of robot base detection in a practical scenario. A point cloud is fed into PV-RCNN++, which produces a score and prediction bounding box. Meanwhile, we evaluate each result by 3D-IOU [60, 61]. This metric, which is widely used in 3D object detection tasks, is determined by computing the volume of the intersection of the predicted and the ground truth bounding box, as illustrated in Fig. 5(a). An example with 0.78 of 3D-IoU is given in Fig. 5(b). The evaluation results are presented in Table 2 where Number indicates the size of evaluation dataset. Based on the experiment results, the average 3D-IoU and score for the test dataset are found to be 0.86 and 0.96. The detection results shown in Table 2 exhibit stability, as indicated by the standard deviation.

In summary, the purpose of 3D detection in our study is to identify the location of the robot base using a bounding box that increases the overlap area with the model of the robot base. Our robot base detection experiment based on PV-RCNN++, a deep learning framework for 3D detection, achieves a prediction result with an average 86% overlap with the ground truth data and a detection score of 0.96. In addition, the average detection time is 0.09 seconds, which can provide approximately 11 RoIs per second. The point cloud of the robot base is extracted as a RoI, as shown in Fig. 6, where the RoI is highlighted in green.

³<https://github.com/open-mmlab/OpenPCDet>

⁴<https://supervise.ly/>

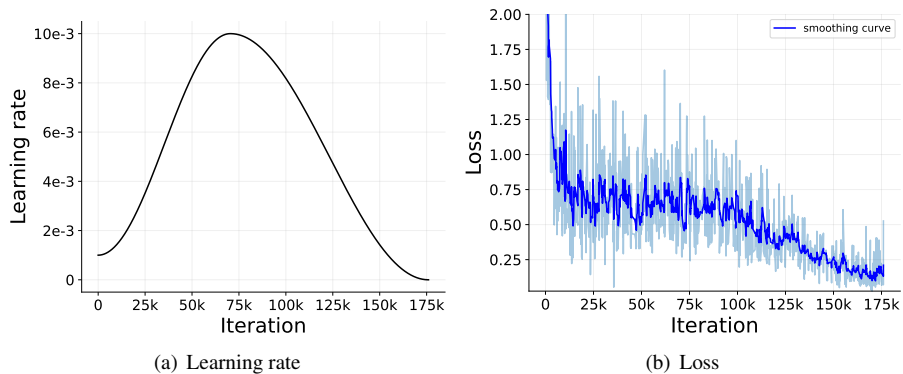


Figure 4: Training performance of PV-RCNN++ for robot base detection in our proposed method.

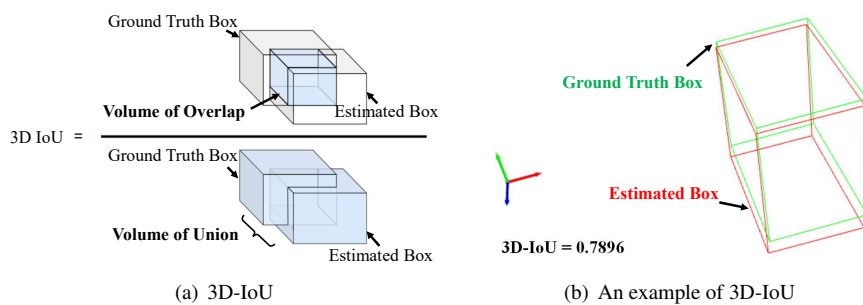


Figure 5: 3D-IoU and an example. An example of 3D-IoU is give on the right where the 3D-IoU is about 0.78.

Table 2: Evaluation result of robot base detection

Item	Standard deviation	Average	Number
Predicted Score	0.081	0.960	468
3D-IoU	0.084	0.866	468

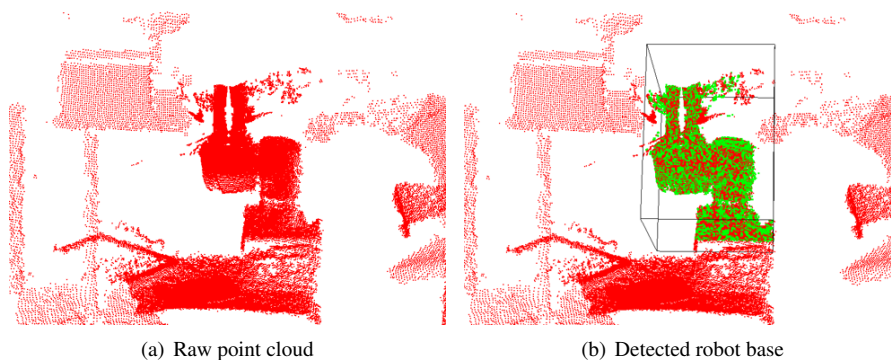


Figure 6: An example of robot base detection: (a) A raw point cloud captured by the 3D camera. (b) A detected result where the robot base is detected with a bounding box and shown in green.

4.2. Robot Base Registration

This section presents the implementation of point cloud registration, including data preparation, training performance and evaluation. The training details of point cloud registration are presented, followed by evaluation details and a comparison with other conventional point cloud registration methods.

The rigid point cloud registration problem can be mathematically described as finding the optimal rigid transformation, $\mathbf{T} = [\mathbf{R} \mid \mathbf{t}]$, that aligns a source point cloud, $P = \{p_i \in \mathbb{R}^3 \mid i = 1 \dots n\}$, with a reference point cloud, $Q = \{q_j \in \mathbb{R}^3 \mid j = 1 \dots m\}$, where \mathbf{R} is a 3×3 rotation matrix and \mathbf{t} is a 3×1 translation vector. The objective is to minimize the distance between corresponding points in the two point clouds as

$$\min_T \sum_{i=1}^n \min_{j=1}^m \|p_i - \mathbf{R}p_j - \mathbf{t}\|_2 \quad (13)$$

where $\|\cdot\|_2$ is the Euclidean norm. The registration point cloud is challenging in our method to the classical registration methods due to the partial data of robot base from the 3D camera. In other words, the data we captured do not fully overlap with the robot base model.

Our study is to find a rigid transformation matrix between a RoI data and the robot base model. To align the RoI of the robot base, which is partial data, with the robot base model, a learning-based framework, PREDATOR [62]⁵, is adopted in our method. It is specifically designed to handle point cloud pairs with low overlap using an overlap-attention block where latent encodings are enabled early information exchange between point clouds. It adopts the attention mechanism to predict overlapping regions for feature sampling. The overlap attention module is developed to reason about each respective overlap region. In this module, a graph neural network (GNN) [63] is used to aggregate and strengthen features contextual relation individually. The final latent feature encoding is yielded by a cross-attention block [64]. In our study, the scanned data as a source point cloud is actually a part of the robot base. The reference point cloud is the robot base model and represented by a point cloud. Moreover, PREDATOR is evaluated and outperformed in 3DMatch [65] and 3DLoMatch datasets, which contain scan pairs with overlaps between 10 and 30%. The network architecture of PREDATOR is illustrated in Fig. 7.

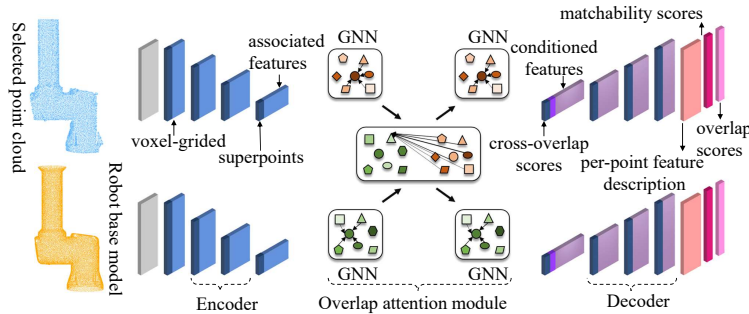


Figure 7: The overall architecture of the PREDATOR framework. A raw point cloud and a selected point cloud are fed to the encoder after a voxel grid filter layer. The superpoints and features are extracted by the encoder. In the overlap attention module, the features are updated with co-contextual information in a series of self-GNN and cross-attention blocks. The overlap and matchability scores are finally transformed by the decoder.

4.2.1. Data Preparation

Generating a high quality robot base registration dataset is a challenging task due to the lack of existing point cloud registration datasets and the difficulty in providing accurate ground truth. To overcome these challenges, we proposed a method that uses the 3D models to generate dataset offline for training. Specifically, we simulated a series of viewpoints where the camera is oriented towards the robot base model. The point clouds from these viewpoints are estimated and selected as source data using hidden surface estimation [66], as illustrated in Fig. 8. In this figure,

⁵<https://github.com/prs-eth/OverlapPredator>

we use UR5e as an example, while our training and evaluation dataset include UR3e, UR5, and UR5e. Therefore, the generation of the dataset can be done through a robot base model offline, rather than capturing data. It can also be used for other types of robot bases. We sample 90 viewpoints within the workspace of the robot and apply arbitrary rotation and translation transformation matrices 10 times to generate a diverse and rich training dataset. The data augmentation process is shown in Fig. 9, using the UR5e as an example, where the reference point cloud is blue and the generated data is black.

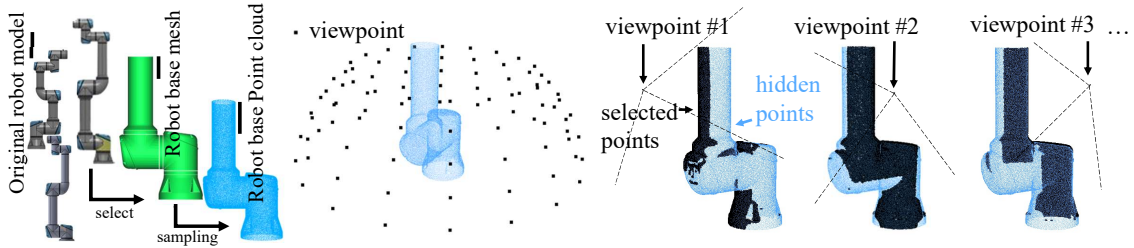


Figure 8: Robot base dataset generation. Given a point cloud of the robot base

, we simulate a number of camera positions in a virtual environment where the scanned data are estimated and selected (black). The selected data are then applied with several arbitrary transformation matrices to be training data.

In our dataset, we have 2700 pairs of aligned point clouds including the robot base from UR3e, UR5 and UR5e. We use 40% of the total data for evaluation, and the rest is used for model training. We use a pre-trained model parameter from the 3DMatch dataset for training efficiency.

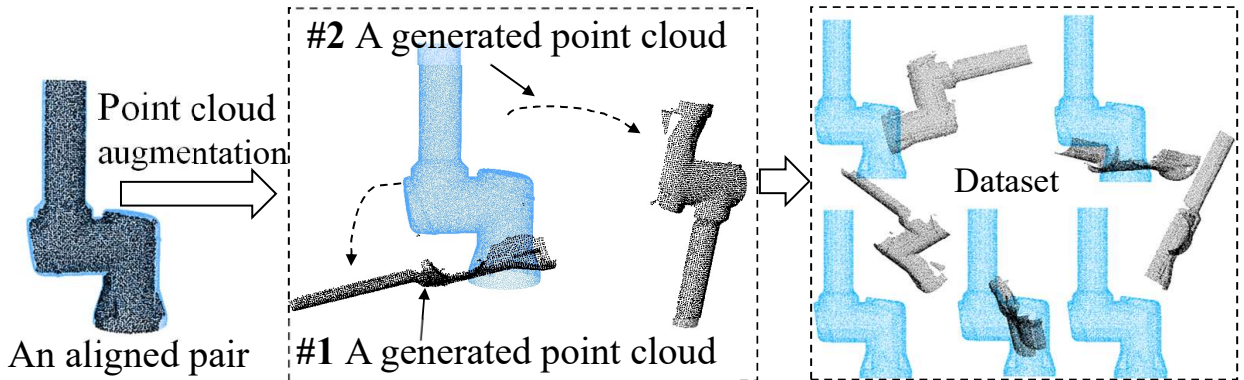


Figure 9: Point cloud augmentation in robot base registration. A point cloud on the left consists of the robot base model (black) and selected points estimated in a virtual viewpoint. After point cloud augmentation, a random transformation matrix is applied to the selected points to produce another point cloud, e.g., two point clouds in black in the middle. On the right are thousands of such point clouds in our database.

4.2.2. Training Performance

We follow the format of 3DMatch to adjust our dataset to be trainable. The PREDATOR is trained with initial learning $5e-4$, momentum 0.8, and weight decay $1e-6$ for 300 epochs. The training process takes approximately 21 hours. In addition, the batch size is set as one due to memory constraints. The other parameters use the same default hyper-parameters as the 3DMatch dataset. During iteration of training, the learning rate and circle loss are reduced as shown in Fig. 10(b), where the learning rate and loss are decreased after a few epochs, as shown in Fig. 10(a) and Fig. 10(b). The recall of overlap is depicted in Fig. 10(c). The best recall weight is saved and utilized for further experiments.

4.2.3. Evaluation

The following metrics are used to evaluate the registration performance:

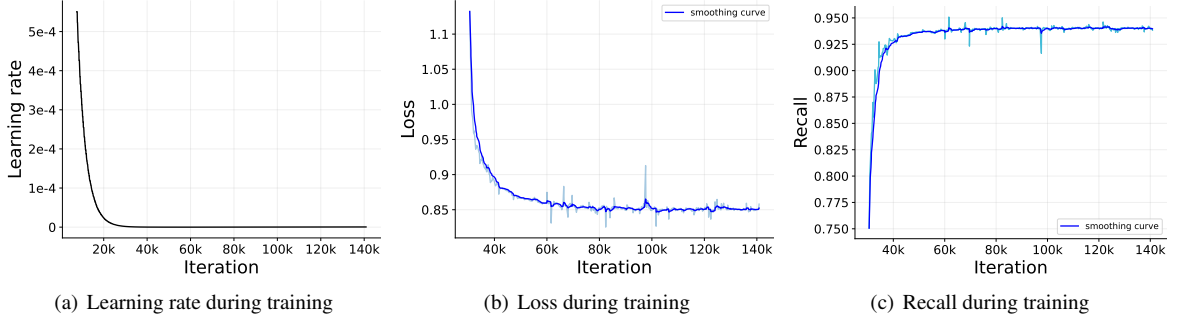


Figure 10: Training performance of robot base registration. PREDATOR is adopted and trained in our method, where learning rate, loss and recall are converged during training process.

- Root Mease Squared Error (RMSE): As a widely used metric [67, 68], it represents the root mean square error between the estimated transformation \mathbf{T}_{est} and the ground truth \mathbf{T}_{gt} . We consider RMSE for rotation and translation matrix as RMSE.T and RMSE.R.
- Relative Rotation Error (RRE) and Relative Translation Error (RTE): RRE [62] is calculated as Eq.14

$$RRE = \arccos \left(\frac{\text{trace}(\mathbf{R}_{est}^T \mathbf{R}_{gt}) - 1}{2} \right) \quad (14)$$

RTE is represented by the Euclidean distance of translation error between \mathbf{T}_{est} and \mathbf{T}_{gt} .

- Rotation Error (RE): RE considers the rotation error in Euclidean norm. Given a 3×3 estimated rotation matrix and a ground truth matrix, we can have vector v_{est} and v_{gt} , both of which contain β , α , and γ :

$$\begin{cases} \beta = \text{atan2}(-R_{3,1}, \text{sqrt}(R_{1,1}^2 + R_{2,1}^2)) \\ \alpha = \text{atan2}\left(\frac{R_{2,1}}{\cos(\beta)}, \frac{R_{1,1}}{\cos(\beta)}\right) \\ \gamma = \text{atan2}\left(\frac{R_{2,1}}{\cos(\beta)}, \frac{R_{3,3}}{\cos(\beta)}\right) \end{cases} \quad (15)$$

where $R_{i,j}$ indicates a element of the i row and i column in the rotation matrix R . RE is obtained as

$$RE = \|v_{est} - v_{gt}\|_2 \quad (16)$$

- Overlap Ratio (OR): OR considers the overlap area of the aligned point cloud and robot base model. The OR is equal to the number of matched points $N_{matched}$ divided by the total number of points of the reference point N_{ref} , as Eq.17.

$$OR = \frac{N_{matched}}{N_{ref}} \quad (17)$$

where N_{ref} is a constant value. Given two point cloud P and Q , the point in source points is considered a matched point as its distance to the nearest one is shorter than τ , which is represented by $1.5 \times$ average distance in our work. The average distance is calculated as the average distance between points in the point cloud. A voxel size-based filtering algorithm is applied to ensure uniform point density for P and Q . The OR for ground truth is about 0.42 with 0.015 voxel size.

To effectively tackle the practical registration problem, it is imperative to conduct experiments to determine the optimal algorithm. We evaluated the performance of PREDATOR and conventional registration algorithms concerning these metrics. These conventional registration algorithms include Iterative Closest Point (ICP), Go-ICP [69], FPFH-based Fast Global Registration (FGR) [70, 71], 4-Points Congruent Sets Registration (4PCS) [72], Coherent Point Drift Registration (CPD) [73], TEASER++ [74]. They are widely used in the registration task due to their outstanding performance in many datasets, such as synthetic range data [75, 76], UWA benchmark [77], 3D Match [65].

An experiment result is shown in Fig. 11, in which we compare PREDATOR to traditional registration methods. Error bars represent the standard deviation and mean value. According to the result presented, PREDATOR exhibits a minor deviation compared to the ground truth, indicating higher reliability. Moreover, the experiments confirm that PREDATOR integrated with a ICP algorithm can refine the registration result in terms of RMSE, RMSE, RTE, RE and OR. Therefore, PREDATOR can be employed in the robot base registration task with relatively high robustness.

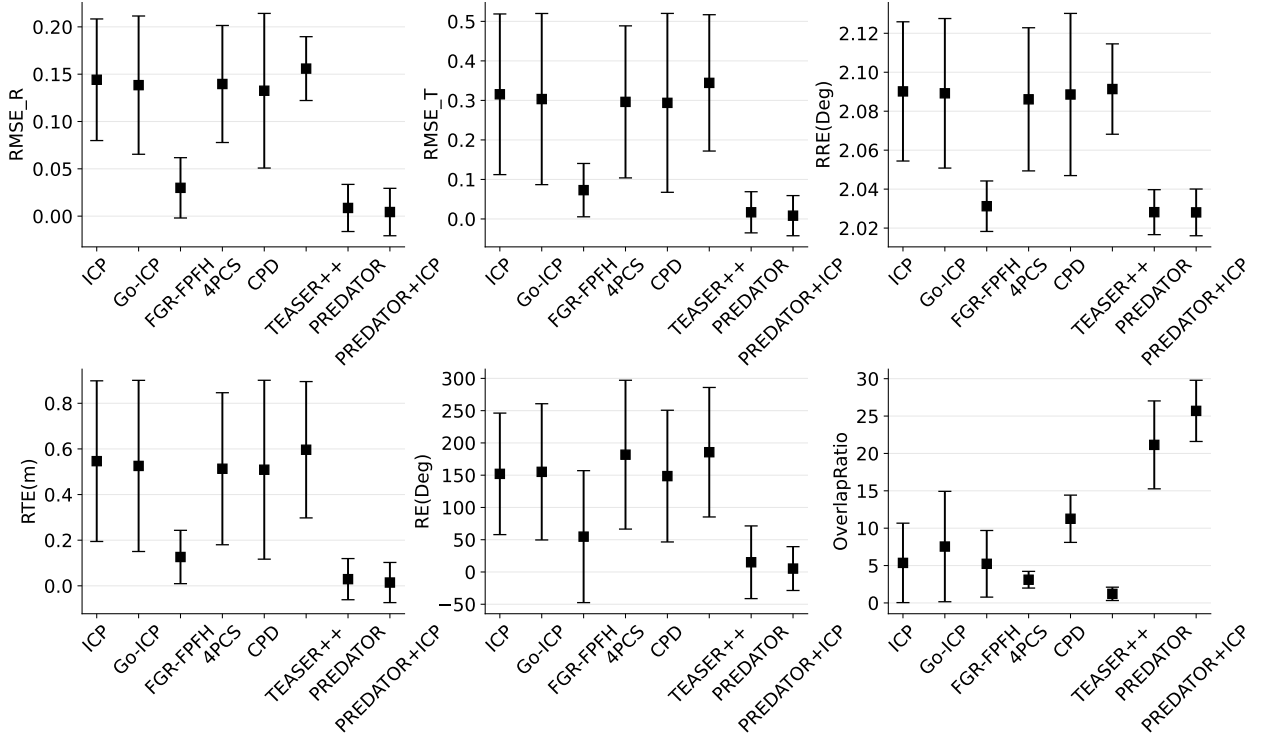


Figure 11: Compared to traditional methods, we convert the registration result into translation and rotation along the X, Y and Z axes. The error bars show the mean value and their lengths show the deviation. The higher the overlap ratio, the better, while the lower the other terms, the better the performance.

In addition, the results of the experiments are summarised in Table 3, where the means of each metric are presented, with emphasis on the best value for each metric. SPS denotes the size of the source data, while TPS denotes the size of the target data. The results show that the combination of the PREDATOR and ICP algorithms results in a more accurate transformation. Furthermore, the runtime of the algorithms is measured on an Intel i7-10510U platform, while TEASER++ and PREDATOR are run on Ubuntu 18.04 with an Intel i9-10850K and an NVIDIA RTX3090. The ICP refinement integrated into PREDATOR benefits from faster computing resources. To accelerate the CPD registration algorithm, a voxel-based filter is applied to reduce the number of points.

The literature on point cloud registration [78, 67, 68] shows that traditional methods cannot achieve the same level of performance as PREDATOR for the following reasons:

- Partial data: Align with the model robot base with only a partial point cloud can lead to local optima. It may affect the CPD registration results because it assumes local isotropic and does not consider structural data information.

Table 3: Training evaluation and comparison of non-learning methods and PREDATOR

Method	RMSE[R]	RMSE[T]	RRE(Deg)	RTE(m)	RE(Deg)	OR(%)	SPS	TPS	T(s)
ICP	0.144	0.315	2.09	0.109	152.058	5.356	3364	12940	0.137
GOICP	0.138	0.303	2.089	0.105	155.189	7.543	3364	12940	3.077
FGR-FPFH	0.03	0.073	2.031	0.025	54.777	5.234	3364	12940	1.401
4PCS	0.14	0.296	2.086	0.103	181.776	3.105	3364	12940	1.092
CPD	0.133	0.294	2.089	0.102	148.577	11.261	630	1694	6.569
TEASER++	0.156	0.344	2.091	0.119	185.603	1.215	3359	12939	0.749
PREDATOR	0.009	0.017	2.028	0.006	15.058	21.145	3358	12838	0.505
PREDATOR+ICP	0.004	0.008	2.028	0.003	5.283	25.695	3358	12857	0.514

- Free-features: The scanned point cloud, a partial point cloud of the robot base, is missing more representative features, which results in a lack of point correspondence obtained from the FPFH feature.
- Poor quality data: The captured data is sometimes low resolution or incomplete due to smooth surfaces on robot joints. It is challenging for 4PCS, which is sensitive to the number of sample points used and its sampling method.
- Outliers: Outliers, such as noise and incorrect points produced by the camera, can significantly impact the registration results.
- Arbitrary position and orientation: Large difference in position and orientation exists in our testing data. It probably impacts the FGR, ICP, and Go-ICP, which are sensitive to initial alignment.

The experiments demonstrate that PREDATOR achieved impressive results on our real-world dataset, outperforming conventional approaches in terms of RMSE, RRE, and other metrics. For example, the registration transformation provided by PREDATOR has an average offset of 0.004 degrees, 8mm, 2.028 degree, 3mm, 5.283 degree, and 25.695% from the ground truth in terms of RMSE.R, RMSE.T, RRE, RTE, RE, and OR. This indicates that PREDATOR yields the smallest deviation from the ground truth transformation matrix and the largest overlap ratio with the UR5e 3D model (point cloud). Moreover, the point cloud registration problem is solved in a mere 0.6 seconds, therefore the total processing time from robot base detection to registration can be less than one second. In the following study, we utilize PREDATOR+ICP to accomplish the robot base registration task.

4.3. Hand-eye Calibration

In the previous sections, two key modules are implemented and evaluated: 1) a 3D detection framework, PV-RCNN++, detects and provides a high-confidence 3D bounding box covering the robot base; 2) a learning-based method, PREDATOR, is utilized to align the RoI with a robot base model, and this alignment is further refined using a ICP algorithm. By training with our data, it outperforms other traditional methods in terms of several metrics, including MESR, RE and RRE. Once we obtain the transformation matrix from the camera to the robot base frame, the hand-eye calibration problem can be solved by Eq.5. A calibrated case is shown in Fig. 12, where each frame is indicated by labels such as “Robot Base” and “3D Camera”. The results show that the position and orientation of the 3D camera is consistent with the real case.

5. Experiments and Discussion

The preceding sections detail the estimation of the robot base pose relative to the 3D camera frame. This section aims to evaluate the reliability and precision of our proposed hand-eye calibration method. It should be noted that it is challenging to assess the absolute precision of hand-eye calibration, as the displacement between the camera and the end-effector is difficult to measure with equipment. [12]. Through we can use hand-eye calibration results to allow robots to interact with the real environment in practical tasks, any errors or large deviations can potentially damage the robot. Therefore, researchers often rely on 3D reconstruction to verify relative accuracy. Here, we include

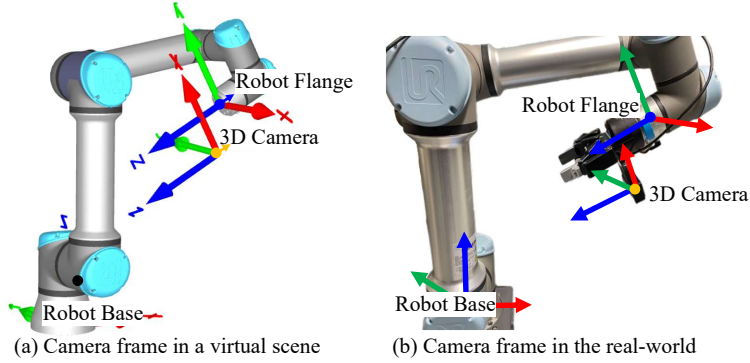


Figure 12: A coordinate system of the camera calculated by eye-in-hand calibration: (a) Camera frame given by our proposed method, shown in a virtual scene. (b) Camera frame in the real world.

3D reconstruction in our experiments to evaluate the performance of our proposed method. In addition, a UR5e collaborative robot, designed to be as safe as possible, is used with a 3D camera mounted on the robot arm.

5.1. Robustness Experiments

Our proposed method can accomplish the hand-eye calibration with a single robot arm movement and point clouds of the robot base. In this section, we conduct the robustness experiment to verify the stability of our proposed method. The term 'stability' in our study refers to the ability of hand-eye calibration to be performed on any suitable joint configuration, rather than being limited to a set of specific joint configurations of the robot arm. While we need to ensure consistency with the 3D model, the -90.0 angle is only set specifically at the second joint. Specifically, we collect 25 point clouds (take ~ 0.5 s) for eye-in-hand calibrations and compare the results at six joint configurations around the robot base, as shown in Fig. 13. We select these joint configurations based on the following rules, which we also recommend for other robots: 1) The robot base should be within the recommended working distance of the camera; 2) The scanned data can include the first and second joints of the robot base, or other joints to avoid the symmetry problem during robot base registration. To achieve the valid transformation matrix, a filter module is developed to retain registration results having a large overlap ratio. The final transformation matrix is then obtained by taking the average of the filtered results. The robot base registration block shown in Fig. 3 is detailed in Fig. 14. We take the eye-in-hand calibration as an example because it is a complex case compared to the eye-to-hand calibration. More specifically, in the eye-hand calibration, the result of the 6D pose estimation of the robot base is its result, while in the eye-hand calibration we also have to consider the forward kinematics. Besides, all the experiments in our study are conducted in an indoor environment.

To ensure the consistency and reliability of our results, we conduct three groups of experiments, denoted as Group 1, Group 2, and Group 3, using six different joint configurations after remounting the camera, as illustrated in Fig. 15. The hand-eye calibration results, shown in Fig. 15(a), demonstrate the transformation matrix between the TCP and the camera represented as Euler angles and translations along the X, Y, and Z axes. Ideally, the translations and rotations along the X, Y, and Z axes should be identical for different joint configurations, as the camera is fixed to the robot arm. However, slight variations in results among the three groups may arise due to mounting errors.

Based on the data shown in Fig. 15(a), the maximum RV of translation along the X, Y and Z axes are 2.471 mm, 3.751 mm and 1.423 mm, which occur in group 3, 2 and 2. The maximum RV of rotation along the X, Y and Z axes are 0.957 degrees, 0.454 degrees and 0.702 degrees, occurring in groups 2, 3 and 2. The average RV is 2.548 mm for translation and 0.704 degrees for rotation throughout the three experimental groups. This indicates that the results estimated at six joint configurations are very close. Furthermore, according to the results in Fig. 15(b), the maximum SD of translation of the X, Y and Z axes occurs in groups 3, 2 and 2. The maximum SD of rotation of the X, Y and Z axes occurs in groups 2, 3 and 2. The average deviation is 0.930 mm for translation and 0.265 degrees for rotation. Given the accuracy of the camera is up to 3 mm within 100 cm and the registration error, the calibration result is acceptable. Therefore, based on the experimental result, a single movement of the robot arm is sufficient.

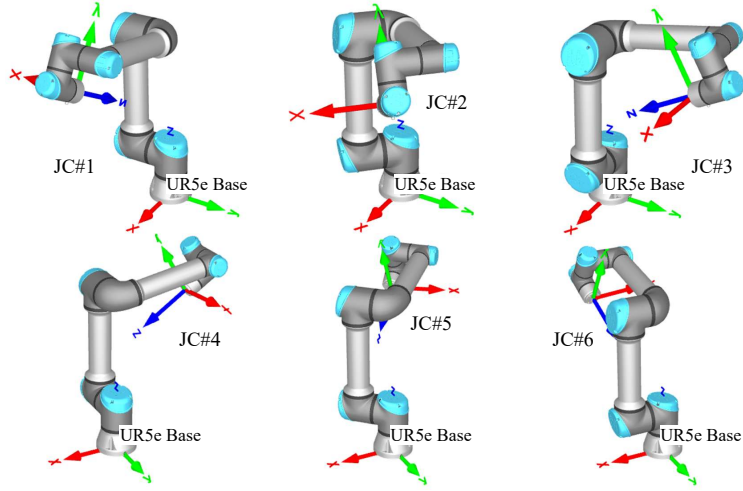


Figure 13: Six joint configurations for hand-eye calibration in which a UR5e is used as an example, and is shown in a virtual environment.

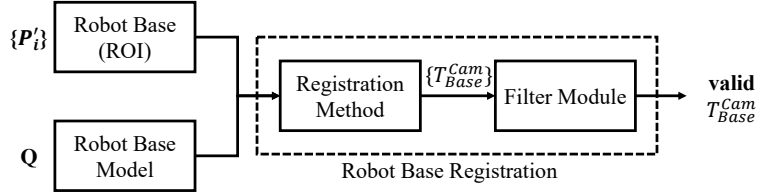


Figure 14: A filter module in the robot base registration where the transformation matrices having large overlap ratio are collected.

The transformation matrix we calibrated between the robot flange and 3D camera is subject to fluctuation due to two primary factors: camera imaging error and registration error. Camera imaging error is the result of systematic error in the 3D camera, leading to deviation in each point cloud representation of the same object surface. In other words, the variation can be smaller once the accuracy of the 3D camera increases. After the process of estimating the camera parameters, the reprojection errors can be used to provide a qualitative measure of the accuracy of the 3D camera. On the other hand, registration error may arise during the final refinement stage using the Iterative Closest Point (ICP) algorithm, potentially converging to a local minimum rather than the global minimum. Furthermore, the accuracy of the ICP algorithm can be affected by the alignment transformation provided by PREDATOR, as ICP is highly sensitive to the initial transformation [68]. In practice, it is essential to carefully consider the similarities between the RoI and the 3D model if the registration results obtained are not as expected.

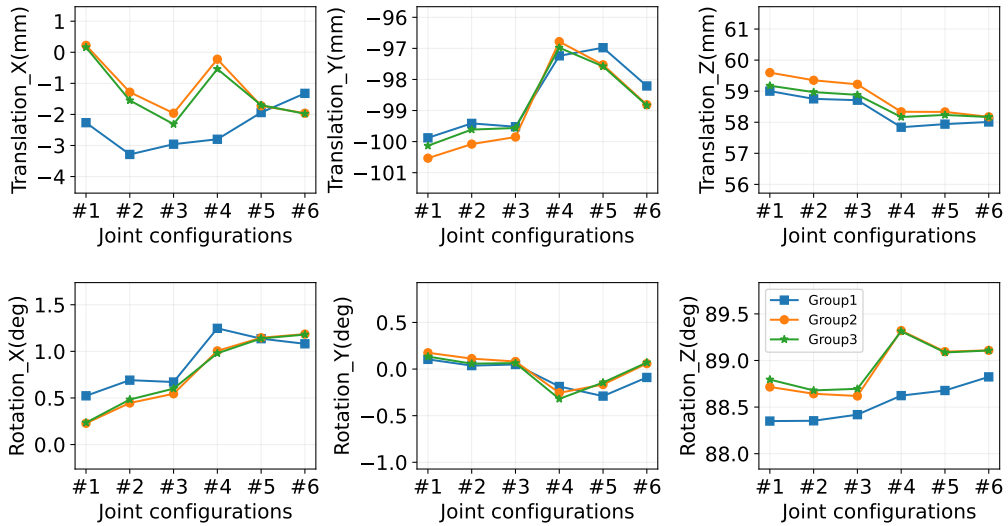
In the following experiment, the transformation matrix calculated at the first joint is utilized to reduce errors arising from camera imaging and environmental factors. This approach considers the average values of translation and rotation, thereby minimizing the impact of fluctuation caused by these factors.

5.2. 3D Reconstruction Experiments

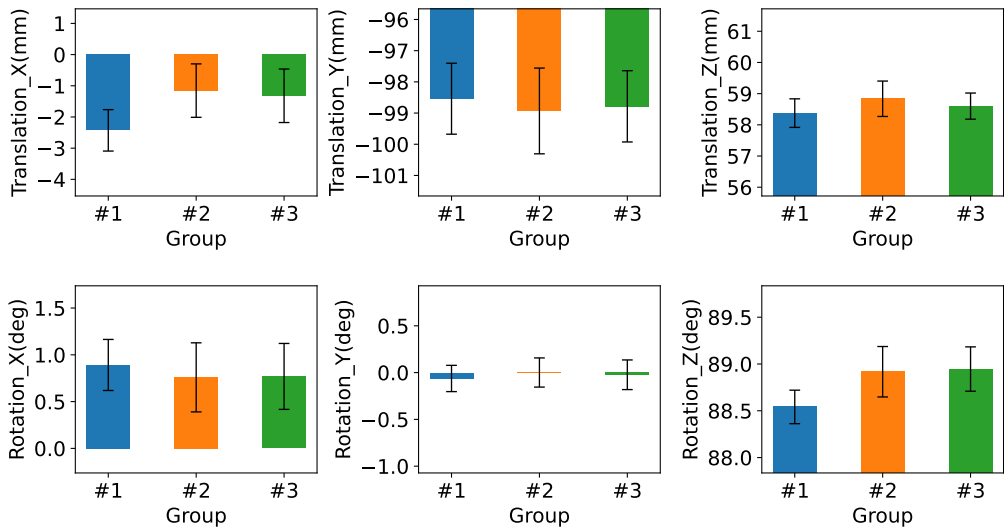
In this section, 3D reconstructions of a plane and a hemisphere are used to evaluate the accuracy of the hand-eye calibration. Specifically, we use a 3D camera mounted on the robotic arm to scan them in white to minimize the impact of color on the maximum measurement range [79].

It is noteworthy that many factors can impact the outcome of 3D reconstruction, including: 1) errors in robotic movement can affect positioning accuracy; 2) incorrect hand-eye calibration can disrupt the relationship between the target object and the robot base, which is evaluated in this section; 3) inaccurate point clouds can also result in an inaccurate representation of the object's surface in the real world.

In 1), it is essential to consider the repeatability and accuracy of the robot during the execution of hand-eye calibration, as the error in \mathbf{A} depends on both the repeatability and accuracy performance of the robot. The official



(a) Hand-eye calibration result calculated under six joint configurations using UR5e. The final transformation matrix from the robot flange to the robot base is represented by the translation and rotation along the X, Y and Z axes. Ideally, each value should be the same under six joint configurations, but may be different for three groups.



(b) Mean value and standard deviation of the calibration results.

Figure 15: Testing error for three groups of experiments. Calibration results including translation and rotation along X, Y and Z axes are estimated under six joint configurations for three groups.

documentation states a repeatability of ± 0.03 mm for the UR5e. On the other hand, the accuracy measures the discrepancy between the desired positioning and the real-world positioning. According to Ryo’s work [80], the positioning accuracy for the UR5e is 0.1 mm, which could potentially have a slight effect on the accuracy of the hand-eye calibration. In addition, factor 3) is noteworthy because the depth accuracy of the 3D camera can reach up to 3 mm within our working distance, which can significantly affect the hand-eye calibration result. Therefore, in order to eliminate the effects of the camera imaging, two types of experiments are conducted:

- **Static test:** We scan the object on a table without any transformations. To assess the fluctuation of camera imaging on the object surface, including the plane surface and hemisphere surface. It can be regarded as a camera imaging error.
- **Dynamic test:** The calibration result is applied to convert captured points to the frame of the robot base. Furthermore, for the transformed point clouds, a refinement registration is incorporated as the ground truth for the 3D reconstruction, namely the Dynamic test with ICP.

In the 3D reconstruction experiments, the plane and hemisphere points are extracted manually. The data acquisition distance is between 50 cm and 60 cm. The plane and hemisphere functions are estimated both by the least squares fit.

5.2.1. Plane Reconstruction

In static testing, a cuboid with a white surface is placed on the table. A total of 40 point clouds are acquired. The experimental setup is illustrated in Fig. 16, where a point cloud is shown as an example on the right.

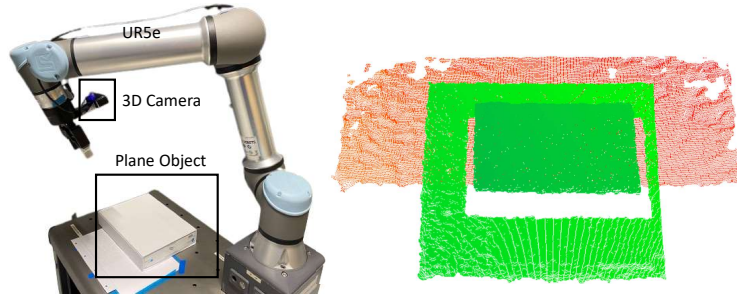


Figure 16: The plane reconstruction setup. To determine the imaging system deviation, the plane of a cuboid is scanned and the angle between the normal vectors and the RMS is estimated.

The angle between normal vectors and RMS are used as metrics in the plane reconstruction. The RMS is defined as

$$RMS = \frac{1}{n} \sum_i^n \| p_i - p_j \|^2, s.t. \| p_i - p_j \|^2 < \tau \quad (18)$$

where τ is given as $1.5 \times$ average distance of the acquired point cloud. The angle is calculated by the normal vector of the top surface and the Z-axis. Ideally, both the RMS and angle are zero. The result of static test is shown in Table 4 which includes the range of values (RV), standard deviation (SD), median and mean value, indicating the distribution and characteristics of our experimental result.

The results show that the camera has random noise on the surface of the object. The average angle and RMS are 0.794 degrees and 1.006 mm. This should be taken into account in the hand-eye calibration result as a systematic error of the 3D camera.

In the dynamic testing phase, we acquired 25 point clouds from various viewpoints by rotating the 3D camera around the cuboid while maintaining a constant working distance. Since these point clouds are captured in the camera frame, they could not be fused into a complete scene, as shown in Fig. 17. On the other hand, the calibrated plane point clouds formed a complete scene and were easily distinguishable. The results of the dynamic test are presented in Table 4, along with a comparison to the static test. Furthermore, to establish a ground truth for the 3D reconstruction

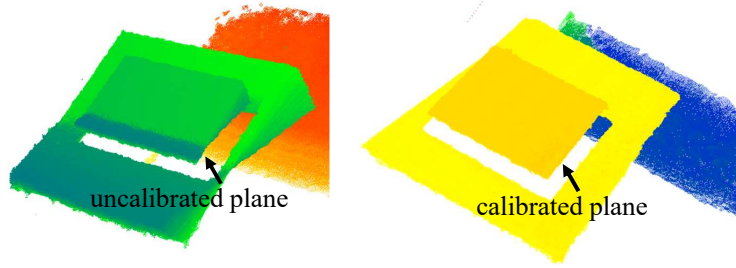


Figure 17: The result of plane reconstruction. The uncalibrated point clouds are on the left, while the calibrated point clouds are shown on the right.

Table 4: Comparison of static and Dynamic tests of the plane reconstruction

	Static test		Dynamic test/ Dynamic test with ICP		Offset	
	Angle (deg)	RMS (mm)	Angle (deg)	RMS (mm)	Angle (deg)	RMS (mm)
Range of values	0.731	1.190	0.599 / 0.833	1.097 / 0.772	0.132 / 0.102	0.093 / 0.418
Standard deviation	0.223	0.237	0.144 / 0.210	0.305 / 0.261	0.079 / 0.013	0.068 / 0.024
Median	0.859	0.970	1.786 / 1.753	1.126 / 1.459	0.927 / 0.894	0.156 / 0.489
Mean	0.794	1.006	1.788 / 1.754	1.182 / 1.505	0.994 / 0.960	0.177 / 0.499

in the dynamic test, where an ICP registration algorithm is applied to the point clouds transformed to the robot base frame, as shown in Table 4, namely Dynamic test with ICP.

The result obtained from static testing is considered as the ground truth. Therefore, the plane points have an offset of 0.994 degree, and a difference of 0.177 mm in terms of angle and RMS compared to the results of static test, indicating a rotation error in the plane reconstruction. Given the offset of 0.960 mm, calculated from the comparison between the dynamic test with ICP and the static test, the obtained result is reliable.

5.2.2. Hemisphere Reconstruction

In static testing, we scanned the hemisphere surface using a 3D camera from a random pose, as shown in Fig. 18. A total of 40 point clouds were captured for the static testing, while 25 point clouds were used for the dynamic testing. Due to the hemisphere shape of the object, we used metrics such as the distance of center points (DC), estimated radius, and RMS for evaluating the reconstruction results. Ideally, the DC and RMS should be zero, and the designed radius for the hemisphere is 75mm.

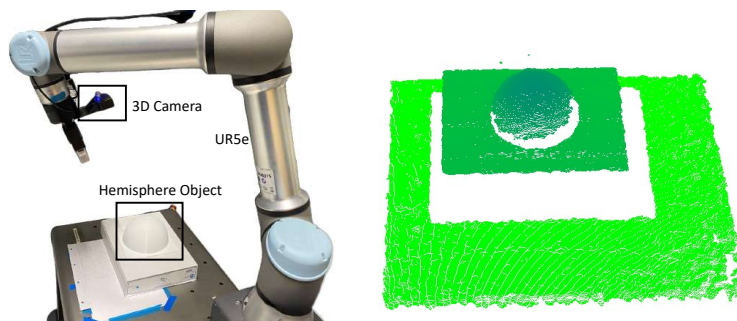


Figure 18: The setup of hemisphere reconstruction where a hemisphere object is placed on the table. The point cloud captured at current pose of robot arm is shown on the right.

Table 5: Comparison of static and Dynamic tests in the hemisphere reconstruction (mm)

	Item	RV	SD	Median	Mean
Static test	Center point(x)	0.125	0.032	97.436	97.450
	Center point(y)	0.087	0.020	-464.726	-464.732
	Center point(z)	0.272	0.063	-15.342	-15.344
	Radius	0.158	0.034	72.709	72.707
	RMS	0.556	0.139	0.733	0.694
	DC	0.207	0.050	0.083	0.095
Dynamic test/ Dynamic test with ICP	Center point(x)	2.320 / 4.185	0.599 / 1.088	96.089 / 97.150	96.291 / 97.321
	Center point(y)	1.516 / 2.430	0.434 / 0.775	-464.095 / -464.062	-464.035 / -463.915
	Center point(z)	2.274 / 2.530	0.503 / 0.669	-14.335 / -14.261	-14.319 / -14.199
	Radius	1.176 / 1.066	0.267 / 0.281	71.940 / 71.970	71.953 / 71.933
	RMS	0.482 / 0.489	0.129 / 0.144	1.230 / 1.304	1.210 / 1.346
	DC	1.965 / 2.218	0.482 / 0.765	1.156 / 2.111	1.140 / 1.959
Offset	Center point(x)	2.196 / 4.060	0.567 / 1.056	1.348 / 0.287	1.159 / 0.129
	Center point(y)	1.429 / 2.344	0.415 / 0.756	0.631 / 0.664	0.697 / 0.816
	Center point(z)	2.002 / 2.258	0.440 / 0.606	1.008 / 1.082	1.025 / 1.146
	Radius	1.018 / 0.908	0.233 / 0.248	0.769 / 0.739	0.754 / 0.774
	RMS	0.074 / 0.068	0.010 / 0.005	0.497 / 0.571	0.517 / 0.652
	DC	1.758 / 2.011	0.432 / 0.716	1.073 / 2.027	1.046 / 1.865

The static testing demonstrates the camera has random noise on the hemisphere surface. The average radius, DC and RMS are estimated to be 72.707 mm, 0.095 mm, and 0.694 mm. In dynamic test, a total of 40 point clouds are captured from various perspectives as the 3D camera rotates around the center of the hemisphere, maintaining a constant working distance. These point clouds are recorded in the camera frame. The calibrated point clouds are then converted into the base frame to reconstruct the complete hemisphere object, as shown in Fig. 19.

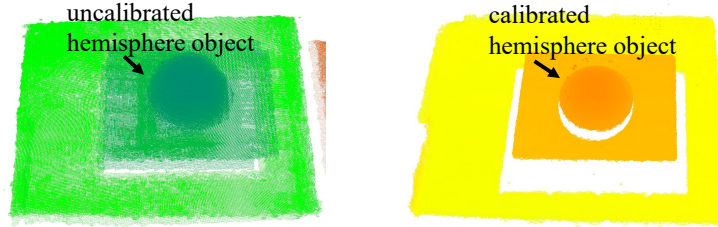


Figure 19: The result of hemisphere reconstruction. The uncalibrated point clouds are on the left, while the calibrated point clouds are shown on the right.

The dynamic testing result is shown in Table 5, where we present a comparison between the static and dynamic tests. We also provide the estimated center point along the X, Y, and Z axes, which are expected to be identical as the hemisphere object remains stationary in both dynamic and static test. The RV, SD, median and mean are also provided to show the distribution of the results of the experiments.

The conclusions drawn from the 3D hemisphere reconstruction experiment are as follows: 1) The calibration result exhibits an offset of 1.046 mm, 0.754 mm and 0.517 mm in DC, radius, and RMS as compared to the results obtained from static test. This offset falls within the acceptable range, considering the 3 mm error from the imaging system; 2) The offsets of 1.159mm, 0.697mm, and 1.025mm along the X, Y, and Z axes indicate a position error of 1.697 mm; 3) Considering the offset results obtained from the dynamic test with ICP and the static test, the calculated offsets are 0.129 mm, 0.816 mm, and 1.146 mm along the X, Y, and Z axes. These values collectively indicate a position error of 1.412 mm, which serves as the ground truth for the 3D reconstitution. In summary, the position error of 1.697

mm is reliable based on the established ground truth of the 3D reconstruction, which is very close to the result of the dynamic test.

5.3. Comparison and Discussion

In the previous sections, we conducted robustness and accuracy experiments. In this section, we compare the position, rotation error and runtime with other conventional hand-eye calibration methods based on 3D vision, as shown in Table 6. These recent studies have demonstrated explicit and excellent experimental results and utilized point clouds during hand-eye calibration. For example, Shiyu [8] introduced a hand-eye calibration method for 3D-sensors that utilizes arbitrary objects. This method achieves the simultaneous registration of multiview point clouds under the robot base frame through iterative refinement of the hand-eye relation. On the other hand, Zhe [24] proposed an eye-in-hand system, which employs a line structured light vision sensor and low-cost planar checkerboard. The calibration process involves capturing a set of images by changing the poses of the robot and calibration target, followed by conducting camera calibration. In the Table 6, *None* indicates that it is not included in this work. It is worth noting that many solutions only measure the algorithm’s processing time and overlook the time spent on robot movement and human assistance, which can significantly increase the overall time required for hand-eye calibration. Our proposed method requires only one movement, which takes approximately 5 seconds.

According to the results presented in Table 6, the position and rotation error of our method is comparable to other methods, except for the method presented by Murali [81]. It is worth mentioning that the X, Y, and Z axes are defined with respect to the robot base frame. This difference could be due to their use of a more precise sensor, a laser profile sensor with a Z-axis resolution of 0.092 to 0.488 mm and a Z-axis repeatability of $\pm 12\mu\text{m}$, while the sensor used in our method has a depth repeatability of less than 3 mm and a point density of 0.9 mm. However, our method shows a faster runtime while maintaining comparable performance. Specifically, our method is twice as fast as the fastest among the other methods.

Table 6: Comparison of other hand-eye calibration methods using 3D point clouds

Method	Position error (mm)			Rotation error (deg)	Runtime (s)	Camera type
Shiyu [8]	1.7			0.4	10.9	Structured-light
Peters [45]	1.77			0.547	15984	Structured-light
Mingyang [9]	(X:0.82	Y:1.22	Z:1.22)	None	1227	Line laser
Murali [81]	(X: 0.701	Y: 0.443	Z: 0.366)	1~2	None	Laser profile
Zhe [24]	(X:1.334	Y:0.511	Z:0.925)	1.231	None	Line laser
Ours	(X:1.159	Y:0.697	Z:1.025)	0.994	<1s + 5 (move)	Structured-light
		1.697				

6. Conclusion

This paper has proposed a novel approach to hand-eye calibration using only point clouds of the robot base. The principle behind this method is simple and effective. Specifically, it estimated a homogeneous transformation matrix between the coordinate frame of the robot base and the end-effector by the 6D pose estimation of the robot base. Learning-based algorithms, including 3D detection and registration, have been used for this purpose. The 3D detection provided a rough location for the robot base given one point cloud, followed by an RoI of the robot base extracted by a bounding box obtained from the detection result. On the one hand, a learning-based algorithm, PV-RCNN++, can provide a prediction result having an average 86% overlap with the ground truth. The robot base can be detected within 0.09 seconds given one point cloud. On the other hand, a learning-based registration framework, PREDATOR, has been exploited to align the RoI with a 3D model of the robot base. Subsequently, the alignment

result is refined using the ICP algorithm. A robot base dataset is selected in a virtual environment using hidden surface estimation. It is therefore possible to extend it to other types of robot bases. The robot base alignment can be achieved in half a second. In addition, it outperforms other traditional registration methods in many metrics, such as RMSE, RRE, RTE, and OR, according to the experiments.

In the robustness experiments, we have conducted three groups of hand-eye calibrations with six different joint configurations. The average deviation for translation and rotation is 0.930 mm and 0.265 degree. In the accuracy experiments, static tests are performed and their results were taken as ground truth. The dynamic tests have then been conducted to evaluate the accuracy of our proposed approach. The results show that the position error is 1.159 mm, 0.697 mm and 1.025 mm along the X, Y and Z axes, which is reliable according to the results of the dynamic test with ICP. In addition, the rotation error is 0.994 degrees according to the reconstruction experiments.

In future studies, the proposed method will be evaluated for its suitability in various industrial applications such as bin-picking, workpiece quality inspection and robotic assembly. We believe that our proposed approach could be a fast and accurate approach for 3D vision based hand-eye calibration.

Acknowledgements The support of Jungner Company and the Wenzhou Major Science and Technology Innovation Project (ZG2022011) is gratefully acknowledged. The authors would like to thank our teammate Yixiong Du for his wonderful collaboration and patient support.

Conflicts of Interest The authors declare that they have no known competing financial interests or personal relationships that could have appeared to influence the work reported in this paper.

Code availability The code and programming generated during and/or analyzed during the current study are available from the corresponding author upon reasonable request.

Authors' Contributions Leihui Li: Methodology, Implementation, Validation, Methodology, Writing Original Draft. Xingyu Yang: Methodology, Validation, Review, and Editing. Riwei Wang and Xuping Zhang*: Supervision, Conceptualization, Methodology, Writing Original Draft.

Declarations

Ethical approval This article does not contain any studies with human participants performed by any of the authors.

Consent to Participate Not applicable.

Consent for Publication Not applicable.

References

- [1] R. Y. Tsai, R. K. Lenz, et al., A new technique for fully autonomous and efficient 3 d robotics hand/eye calibration, *IEEE Transactions on robotics and automation* 5 (3) (1989) 345–358.
- [2] R. Horaud, F. Dornaika, Hand-eye calibration, *The international journal of robotics research* 14 (3) (1995) 195–210.
- [3] K. H. Strobl, G. Hirzinger, Optimal hand-eye calibration, in: 2006 IEEE/RSJ international conference on intelligent robots and systems, IEEE, 2006, pp. 4647–4653.
- [4] M. Dinham, G. Fang, A low cost hand-eye calibration method for arc welding robots, in: 2009 IEEE international conference on robotics and biomimetics (ROBIO), IEEE, 2009, pp. 1889–1893.
- [5] Y. Motai, A. Kosaka, Hand-eye calibration applied to viewpoint selection for robotic vision, *IEEE Transactions on Industrial Electronics* 55 (10) (2008) 3731–3741.
- [6] W.-L. Li, H. Xie, G. Zhang, S.-J. Yan, Z.-P. Yin, Hand-eye calibration in visually-guided robot grinding, *IEEE transactions on cybernetics* 46 (11) (2015) 2634–2642.
- [7] P. Liang, W. Lin, G. Luo, C. Zhang, Research of hand-eye system with 3d vision towards flexible assembly application, *Electronics* 11 (3) (2022) 354.
- [8] S. Xing, F. Jing, M. Tan, Reconstruction based hand-eye calibration using arbitrary objects, *IEEE Transactions on Industrial Informatics* (2022).
- [9] M. Li, Z. Du, X. Ma, W. Dong, Y. Gao, A robot hand-eye calibration method of line laser sensor based on 3d reconstruction, *Robotics and Computer-Integrated Manufacturing* 71 (2021) 102136.
- [10] N. Andreff, R. Horaud, B. Espiau, On-line hand-eye calibration, in: *Second International Conference on 3-D Digital Imaging and Modeling* (Cat. No. PR00062), IEEE, 1999, pp. 430–436.
- [11] K. Koide, E. Menegatti, General hand-eye calibration based on reprojection error minimization, *IEEE Robotics and Automation Letters* 4 (2) (2019) 1021–1028.
- [12] I. Enebuse, M. Foo, B. S. K. K. Ibrahim, H. Ahmed, F. Supmak, O. S. Eyobu, A comparative review of hand-eye calibration techniques for vision guided robots, *IEEE Access* 9 (2021) 113143–113155.
- [13] J. Jiang, X. Luo, Q. Luo, L. Qiao, M. Li, An overview of hand-eye calibration, *The International Journal of Advanced Manufacturing Technology* 119 (1-2) (2022) 77–97.

- [14] I. Enebase, B. K. K. Ibrahim, M. Foo, R. S. Matharu, H. Ahmed, Accuracy evaluation of hand-eye calibration techniques for vision-guided robots, *Plos one* 17 (10) (2022) e0273261.
- [15] L. Huang, F. Da, S. Gai, Research on multi-camera calibration and point cloud correction method based on three-dimensional calibration object, *Optics and Lasers in Engineering* 115 (2019) 32–41.
- [16] K.-H. Lee, H.-S. Kim, S.-J. Lee, S.-W. Choo, S.-M. Lee, K.-T. Nam, High precision hand-eye self-calibration for industrial robots, in: 2018 International Conference on Electronics, Information, and Communication (ICEIC), IEEE, 2018, pp. 1–2.
- [17] H. Kato, M. Billinghurst, Marker tracking and hmd calibration for a video-based augmented reality conferencing system, in: Proceedings 2nd IEEE and ACM International Workshop on Augmented Reality (IWAR'99), IEEE, 1999, pp. 85–94.
- [18] B. Atcheson, F. Heide, W. Heidrich, Caltag: High precision fiducial markers for camera calibration., in: *VMV*, Vol. 10, 2010, pp. 41–48.
- [19] X. Xu, D. Zhu, H. Zhang, S. Yan, H. Ding, Tcp-based calibration in robot-assisted belt grinding of aero-engine blades using scanner measurements, *The International Journal of Advanced Manufacturing Technology* 90 (2017) 635–647.
- [20] S. Levine, P. Pastor, A. Krizhevsky, J. Ibarz, D. Quillen, Learning hand-eye coordination for robotic grasping with deep learning and large-scale data collection, *The International journal of robotics research* 37 (4-5) (2018) 421–436.
- [21] L. Ma, P. Bazzoli, P. M. Sammons, R. G. Landers, D. A. Bristow, Modeling and calibration of high-order joint-dependent kinematic errors for industrial robots, *Robotics and Computer-Integrated Manufacturing* 50 (2018) 153–167.
- [22] J. Wu, M. Wang, Y. Jiang, B. Yi, R. Fan, M. Liu, Simultaneous hand-eye/robot-world/camera-imu calibration, *IEEE/ASME Transactions on Mechatronics* 27 (4) (2021) 2278–2289.
- [23] H. Yu, Y. Huang, D. Zheng, L. Bai, J. Han, Three-dimensional shape measurement technique for large-scale objects based on line structured light combined with industrial robot, *Optik* 202 (2020) 163656.
- [24] Z. Wang, J. Fan, F. Jing, S. Deng, M. Zheng, M. Tan, An efficient calibration method of line structured light vision sensor in robotic eye-in-hand system, *IEEE Sensors Journal* 20 (11) (2020) 6200–6208.
- [25] Z. Xie, P. Zong, P. Yao, P. Ren, Calibration of 6-dof industrial robots based on line structured light, *Optik* 183 (2019) 1166–1178.
- [26] Y. Shiu, S. Ahmad, Calibration of wrist-mounted robotic sensors by solving homogeneous transform equations of the form $ax=xb$, *IEEE Transactions on Robotics and Automation* 5 (1) (1989) 16–29. doi:10.1109/70.88014.
- [27] H. Zhuang, Z. S. Roth, R. Sudhakar, Simultaneous robot/world and tool/flange calibration by solving homogeneous transformation equations of the form $ax=yb$, *IEEE Transactions on Robotics and Automation* 10 (4) (1994) 549–554.
- [28] F. Dornaika, R. Horaud, Simultaneous robot-world and hand-eye calibration, *IEEE transactions on Robotics and Automation* 14 (4) (1998) 617–622.
- [29] L. Wu, J. Wang, L. Qi, K. Wu, H. Ren, M. Q.-H. Meng, Simultaneous hand-eye, tool-flange, and robot-robot calibration for comanipulation by solving the $axb=ycz$ problem, *IEEE Transactions on robotics* 32 (2) (2016) 413–428.
- [30] Y. Qin, P. Geng, B. Lv, Y. Meng, Z. Song, J. Han, Simultaneous calibration of the hand-eye, flange-tool and robot-robot relationship in dual-robot collaboration systems, *Sensors* 22 (5) (2022) 1861.
- [31] X. Zhi, S. Schwertfeger, Simultaneous hand-eye calibration and reconstruction, in: 2017 IEEE/RSJ International Conference on Intelligent Robots and Systems (IROS), IEEE, 2017, pp. 1470–1477.
- [32] I. Ali, O. Suominen, A. Gotchev, E. R. Morales, Methods for simultaneous robot-world-hand-eye calibration: A comparative study, *Sensors* 19 (12) (2019) 2837.
- [33] J. Schmidt, F. Vogt, H. Niemann, Calibration-free hand-eye calibration: a structure-from-motion approach, in: *Pattern Recognition: 27th DAGM Symposium, Vienna, Austria, August 31-September 2, 2005. Proceedings 27*, Springer, 2005, pp. 67–74.
- [34] M. Antonello, A. Gobbi, S. Michieletto, S. Ghidoni, E. Menegatti, A fully automatic hand-eye calibration system, in: 2017 European conference on mobile robots (ECMR), IEEE, 2017, pp. 1–6.
- [35] S. Garrido-Jurado, R. Muñoz-Salinas, F. J. Madrid-Cuevas, M. J. Marín-Jiménez, Automatic generation and detection of highly reliable fiducial markers under occlusion, *Pattern Recognition* 47 (6) (2014) 2280–2292.
- [36] J. Abdullah, K. Martinez, Camera self-calibration for the artoolkit, in: *The First IEEE International Workshop Augmented Reality Toolkit*, IEEE, 2002, pp. 5–pp.
- [37] M. Fiala, Artag, a fiducial marker system using digital techniques, in: 2005 IEEE Computer Society Conference on Computer Vision and Pattern Recognition (CVPR'05), Vol. 2, IEEE, 2005, pp. 590–596.
- [38] S. Lee, S. Ro, A self-calibration model for hand-eye systems with motion estimation, *Mathematical and computer modelling* 24 (5-6) (1996) 49–77.
- [39] G.-Q. Wei, K. Arbter, G. Hirzinger, Active self-calibration of robotic eyes and hand-eye relationships with model identification, *IEEE Transactions on Robotics and Automation* 14 (1) (1998) 158–166.
- [40] J. Heller, M. Havlena, A. Sugimoto, T. Pajdla, Structure-from-motion based hand-eye calibration using l1 minimization, in: *CVPR 2011*, IEEE, 2011, pp. 3497–3503.
- [41] N. Andreff, R. Horaud, B. Espiau, Robot hand-eye calibration using structure-from-motion, *The International Journal of Robotics Research* 20 (3) (2001) 228–248.
- [42] K. Pachtrachai, M. Allan, V. Pawar, S. Hailes, D. Stoyanov, Hand-eye calibration for robotic assisted minimally invasive surgery without a calibration object, in: 2016 IEEE/RSJ International Conference on Intelligent Robots and Systems (IROS), IEEE, 2016, pp. 2485–2491.
- [43] W. Chen, J. Du, W. Xiong, Y. Wang, S. Chia, B. Liu, J. Cheng, Y. Gu, A noise-tolerant algorithm for robot-sensor calibration using a planar disk of arbitrary 3-d orientation, *IEEE Transactions on Automation Science and Engineering* 15 (1) (2016) 251–263.
- [44] M. Wagner, P. Heß, S. Reitelshöfer, J. Franke, Self-calibration method for a robotic based 3d scanning system, in: 2015 IEEE 20th Conference on Emerging Technologies & Factory Automation (ETFA), IEEE, 2015, pp. 1–6.
- [45] A. Peters, Robot self-calibration using actuated 3d sensors, arXiv preprint arXiv:2206.03430 (2022).
- [46] T. E. Lee, J. Tremblay, T. To, J. Cheng, T. Mosier, O. Kroemer, D. Fox, S. Birchfield, Camera-to-robot pose estimation from a single image, in: 2020 IEEE International Conference on Robotics and Automation (ICRA), IEEE, 2020, pp. 9426–9432.
- [47] J. Bohg, J. Romero, A. Herzog, S. Schaal, Robot arm pose estimation through pixel-wise part classification, in: 2014 IEEE International Conference on Robotics and Automation (ICRA), IEEE, 2014, pp. 3143–3150.

- [48] J. M. Wong, V. Kee, T. Le, S. Wagner, G.-L. Mariottini, A. Schneider, L. Hamilton, R. Chipalkatty, M. Hebert, D. M. Johnson, et al., Segicp: Integrated deep semantic segmentation and pose estimation, in: 2017 IEEE/RSJ International Conference on Intelligent Robots and Systems (IROS), IEEE, 2017, pp. 5784–5789.
- [49] F. C. Park, B. J. Martin, Robot sensor calibration: solving $ax = xb$ on the euclidean group, *IEEE Transactions on Robotics and Automation* 10 (5) (1994) 717–721.
- [50] K. Daniilidis, Hand-eye calibration using dual quaternions, *The International Journal of Robotics Research* 18 (3) (1999) 286–298.
- [51] K. Daniilidis, E. Bayro-Corrochano, The dual quaternion approach to hand-eye calibration, in: *Proceedings of 13th International Conference on Pattern Recognition*, Vol. 1, IEEE, 1996, pp. 318–322.
- [52] X. Wang, H. Song, Optimal robot-world and hand-eye calibration with rotation and translation coupling, *Robotica* 40 (9) (2022) 2953–2968.
- [53] Z. Zhao, Y. Liu, A hand-eye calibration algorithm based on screw motions, *Robotica* 27 (2) (2009) 217–223.
- [54] J. Hua, L. Zeng, Hand-eye calibration algorithm based on an optimized neural network, in: *Actuators*, Vol. 10, MDPI, 2021, p. 85.
- [55] D. Girardeau-Montaut, Cloudcompare, France: EDF R&D Telecom ParisTech 11 (2016).
- [56] S. Shi, L. Jiang, J. Deng, Z. Wang, C. Guo, J. Shi, X. Wang, H. Li, Pv-rnn++: Point-voxel feature set abstraction with local vector representation for 3d object detection, *International Journal of Computer Vision* (2022) 1–21.
- [57] S. Shi, C. Guo, L. Jiang, Z. Wang, J. Shi, X. Wang, H. Li, Pv-rnn: Point-voxel feature set abstraction for 3d object detection, in: *Proceedings of the IEEE/CVF Conference on Computer Vision and Pattern Recognition*, 2020, pp. 10529–10538.
- [58] A. Geiger, P. Lenz, C. Stiller, R. Urtasun, Vision meets robotics: The kitti dataset, *The International Journal of Robotics Research* 32 (11) (2013) 1231–1237.
- [59] P. Sun, H. Kretschmar, X. Dotiwalla, A. Chouard, V. Patnaik, P. Tsui, J. Guo, Y. Zhou, Y. Chai, B. Caine, et al., Scalability in perception for autonomous driving: Waymo open dataset, in: *Proceedings of the IEEE/CVF conference on computer vision and pattern recognition*, 2020, pp. 2446–2454.
- [60] S. Shi, X. Wang, H. Li, Pointcnn: 3d object proposal generation and detection from point cloud, in: *Proceedings of the IEEE/CVF conference on computer vision and pattern recognition*, 2019, pp. 770–779.
- [61] Z. Yang, Y. Sun, S. Liu, X. Shen, J. Jia, Std: Sparse-to-dense 3d object detector for point cloud, in: *Proceedings of the IEEE/CVF international conference on computer vision*, 2019, pp. 1951–1960.
- [62] S. Huang, Z. Gojcic, M. Usvatsov, A. Wieser, K. Schindler, Predator: Registration of 3d point clouds with low overlap, in: *Proceedings of the IEEE/CVF Conference on computer vision and pattern recognition*, 2021, pp. 4267–4276.
- [63] Y. Wang, Y. Sun, Z. Liu, S. E. Sarma, M. M. Bronstein, J. M. Solomon, Dynamic graph cnn for learning on point clouds, *Acm Transactions On Graphics (tog)* 38 (5) (2019) 1–12.
- [64] P.-E. Sarlin, D. DeTone, T. Malisiewicz, A. Rabinovich, Superglue: Learning feature matching with graph neural networks, in: *Proceedings of the IEEE/CVF conference on computer vision and pattern recognition*, 2020, pp. 4938–4947.
- [65] A. Zeng, S. Song, M. Nießner, M. Fisher, J. Xiao, T. Funkhouser, 3dmatch: Learning the matching of local 3d geometry in range scans, in: *CVPR*, Vol. 1, 2017, p. 4.
- [66] L. Carpenter, The a-buffer, an antialiased hidden surface method, in: *Proceedings of the 11th annual conference on Computer graphics and interactive techniques*, 1984, pp. 103–108.
- [67] L. Li, R. Wang, X. Zhang, A tutorial review on point cloud registrations: principle, classification, comparison, and technology challenges, *Mathematical Problems in Engineering* 2021 (2021) 1–32.
- [68] X. Huang, G. Mei, J. Zhang, R. Abbas, A comprehensive survey on point cloud registration, *arXiv preprint arXiv:2103.02690* (2021).
- [69] J. Yang, H. Li, D. Campbell, Y. Jia, Go-icp: A globally optimal solution to 3d icp point-set registration, *IEEE transactions on pattern analysis and machine intelligence* 38 (11) (2015) 2241–2254.
- [70] Q.-Y. Zhou, J. Park, V. Koltun, Fast global registration, in: *Computer Vision—ECCV 2016: 14th European Conference, Amsterdam, The Netherlands, October 11–14, 2016, Proceedings, Part II 14*, Springer, 2016, pp. 766–782.
- [71] R. B. Rusu, N. Blodow, M. Beetz, Fast point feature histograms (fpfh) for 3d registration, in: *2009 IEEE international conference on robotics and automation*, IEEE, 2009, pp. 3212–3217.
- [72] N. Mellado, D. Aiger, N. J. Mitra, Super 4pcs fast global pointcloud registration via smart indexing, in: *Computer graphics forum*, Vol. 33, Wiley Online Library, 2014, pp. 205–215.
- [73] A. Myronenko, X. Song, Point set registration: Coherent point drift, *IEEE transactions on pattern analysis and machine intelligence* 32 (12) (2010) 2262–2275.
- [74] H. Yang, J. Shi, L. Carlone, Teaser: Fast and certifiable point cloud registration, *IEEE Transactions on Robotics* 37 (2) (2020) 314–333.
- [75] R. Kolluri, J. R. Shewchuk, J. F. O’Brien, Spectral surface reconstruction from noisy point clouds, in: *Proceedings of the 2004 Eurographics/ACM SIGGRAPH symposium on Geometry processing*, 2004, pp. 11–21.
- [76] B. Curless, M. Levoy, A volumetric method for building complex models from range images, in: *Proceedings of the 23rd annual conference on Computer graphics and interactive techniques*, 1996, pp. 303–312.
- [77] A. S. Mian, M. Bennamoun, R. Owens, Three-dimensional model-based object recognition and segmentation in cluttered scenes, *IEEE transactions on pattern analysis and machine intelligence* 28 (10) (2006) 1584–1601.
- [78] F. Pomerleau, F. Colas, R. Siegwart, et al., A review of point cloud registration algorithms for mobile robotics, *Foundations and Trends® in Robotics* 4 (1) (2015) 1–104.
- [79] C. Nahler, C. Steger, N. Druml, Quantitative and qualitative evaluation methods of automotive time of flight based sensors, in: *2020 23rd Euromicro Conference on Digital System Design (DSD)*, IEEE, 2020, pp. 651–659.
- [80] R. Okumura, N. Nishio, T. Taniguchi, Tactile-sensitive newtonianvae for high-accuracy industrial connector insertion, in: *2022 IEEE/RSJ International Conference on Intelligent Robots and Systems (IROS)*, 2022, pp. 4625–4631. [doi:10.1109/IROS47612.2022.9981610](https://doi.org/10.1109/IROS47612.2022.9981610).
- [81] P. K. Murali, I. Sorrentino, A. Rendiniello, C. Fantacci, E. Villagrossi, A. Polo, A. Ardesi, M. Maggiali, L. Natale, D. Pucci, et al., In situ translational hand-eye calibration of laser profile sensors using arbitrary objects, in: *2021 IEEE International Conference on Robotics and Automation (ICRA)*, IEEE, 2021, pp. 11067–11073.